Beating 1 Sievert: Optimal Radiation Shielding of Astronauts on a Mission to Mars

AGU ADVANCING EARTH AND SPACE SCIENCE

Space Weather

RESEARCH ARTICLE
10.1029/2021SW002749

Key Points:

- Space missions to Mars should be scheduled to be launched during solar max
- Optimal spacecraft shielding is ~30 g/cm^2, which allows long-duration flights of ~4 years
- Increase of shielding thickness beyond ~30 g/cm^2 results in dose increase

Correspondence to:

M. I. Dobynde and Y. Y. Shprits,
mikhail.dobynde@skolkovotech.ru;
yshprits@gfz-potsdam.de

Citation:

Dobynde, M. I., Shprits, Y. Y., Drozdov, A. Y., Hoffman, J., & Li, J. (2021). Beating 1 sievert: Optimal radiation shielding of astronauts on a mission to Mars. *Space Weather*, *19*, e2021SW002749. https://doi.org/10.1029/2021SW002749

Received 25 FEB 2021
Accepted 5 AUG 2021

Beating 1 Sievert: Optimal Radiation Shielding of Astronauts on a Mission to Mars

M. I. Dobynde[1,2,3,4], Y. Y. Shprits[5,6,7], A. Y. Drozdov[7], J. Hoffman[8], and Ju Li[9]

[1]Skolkovo Institute of Science and Technology, Moscow, Russia, [2]Institute of Biomedical Problems, Russian Academy of Science, Moscow, Russia, [3]Skobeltsyn Institute of Nuclear Physics, Moscow State University, Moscow, Russia, [4]School of Earth and Space Sciences, University of Science and Technology of China, Hefei, China, [5]GFZ German Research Centre for Geosciences, Helmholtz Centre Potsdam, Potsdam, Germany, [6]Institute of Physics and Astronomy, University of Potsdam, Potsdam, Germany, [7]Department of Earth Planetary and Space Sciences, University of California, Los Angeles, Los Angeles, CA, USA, [8]Department of Aeronautics and Astronautics, Massachusetts Institute of Technology, Cambridge, MA, USA, [9]Department of Nuclear Science and Engineering, Massachusetts Institute of Technology, Cambridge, MA, USA

Abstract Space radiation is one of the main concerns in planning long-term human space missions. There are two main types of hazardous radiation: solar energetic particles (SEP) and galactic cosmic rays (GCR). The intensity and evolution of both depends on solar activity. GCR activity is most enhanced during solar minimum and lowest during solar maximum. The reduction of GCRs is alagging behind solar activity only by 6–12 month. SEP probability and intensity are maximized during solar maximum and are minimized during solar minimum. In this study, we combine models of the particle environment arising due to SEP and GCR with Monte Carlo simulations of radiation propagation inside a spacecraft and phantom. We include 28 fully ionized GCR elements from hydrogen to nickel and consider protons and nine ion species to model the SEP irradiation. Our calculations demonstrate that the optimal time for a flight to Mars would be launching the mission at solar maximum, and that the flight duration should not exceed approximately 4 years.

Plain Language Summary Space particle radiation is one of the main concerns in planning long-term human space missions. There are two main types of hazardous particle radiation: (a) solar energetic particles (SEP) originating from the Sun and (b) galactic cosmic rays (GCR) that come from the distant galaxies in space. Fluxes in particles of solar origin maximize during solar maximum when particles originating from the distant galaxies are more efficiently deflected from the solar system during times when the sun is active. Our calculations clearly demonstrate that the best time for launching a human space flight to Mars is during the solar maximum, as it is possible to shield from SEP particles. Our simulations show that an increase in shielding creates an increase in secondary radiation produced by the most energetic GCR, which results in a higher dose, introducing a limit to a mission duration. We estimate that a potential mission to Mars should not exceed approximately 4 years. This study shows that while space radiation imposes strict limitations and presents technological difficulties for the human mission to Mars, such a mission is still viable.

1. Introduction

Exposure of astronauts to space radiation is one of the major barriers to human exploration of the solar system and long-duration human space flights (Cucinotta et al., 2013; Hassler et al., 2014; Zeitlin et al., 2013). In Low-Earth Orbit, astronauts are protected from high-energy charged particle radiation by the Earth's body and magnetic field. However, outside of the magnetosphere, the spacecraft is exposed to particle radiation originating from the Sun, distant stars, and galaxies.

There are two main types of cosmic radiation inside the solar system: Galactic cosmic rays (GCR) and solar energetic particles (SEP). GCR particles originate from the interstellar medium and diffuse inside the heliosphere, forming a spatially homogeneous and angularly isotropic particle flux. GCR comprise 2% of electrons and 98% of baryons, which are fully ionized ions, consisting of 84% protons and 14% alpha particles. Heavy ions (high charge (Z) and energy (E; HZE) particles) make up only 2% of the GCR flux (Nymmik

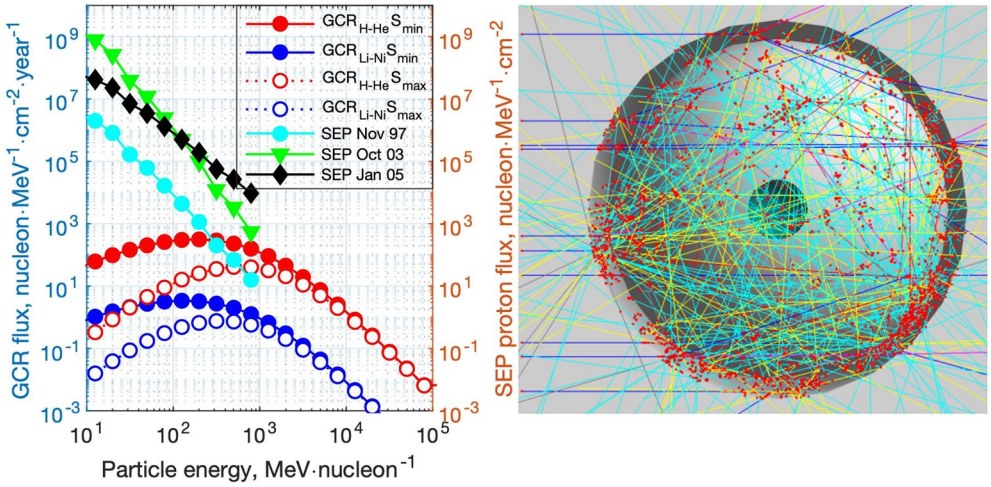

Figure 1. (a) Differential energy spectra of particle flux of various particle species in the interplanetary space near the Earth: galactic cosmic ray particles according to Matthiä, Berger, Mrigakshi, and Reitz (2013): hydrogen and helium (red curve) and heavy ions (blue curve); the proton flux due to the solar particle event (Evaluated Solar Energetic Particle Data, 2018): September 1997 (cyan curve), October 2003 (green curve), and January 2005 (black curve). (b) Illustration of numeric simulations. The spherical aluminum shell (gray) and the spherical water phantom inside it (turquoise) are illuminated with unidirectional 3 GeV protons (blue), which are generated on a circular planar source on the left. Red dots show particle-matter interaction points. Secondary gamma-rays are shown in cyan, neutrons in yellow, protons on blue, leptons in red, and pions in magenta.

et al., 1992). SEP on the other hand, consist mainly of protons and are ejected from the surface of the Sun during solar flares, propagating outward into the solar system.

Both GCR and SEP intensities vary during the 11-years solar cycle. SEP event probability and intensity decrease during solar activity minima (min) and increase during maxima (max). The dependence of GCR on solar activity is related to the strength of the solar wind (Forbush, 1958). During solar min, GCR fluxes increase, while during solar max, GCR fluxes are lower. There are several empirical models (Golge et al., 2015; Matthiä, Berger, Mrigakshi, & Reitz, 2013; Nymmik et al., 1996) that describe GCR particle spectra according to solar activity. The GCR models provide the evolution of electron, proton, and ion fluxes with a relatively high accuracy that is, sufficient for the prediction of long-term trends in particle flux intensities.

Unlike persistent GCR radiation, SEP events are sporadic. Prediction of the SEP event timing, strength, and direction is an extremely challenging task, as the dynamics of the active regions on the Sun and flare generation are not fully understood. Different SEP events have different risk levels for space missions because of the variations in particle spectra. The common feature for SEP spectra is the exponential decrease of particle fluence with energy. Most of the particles have an energy less than approximately several hundred MeV (Figure 1a). It has been shown (Hu et al., 2009) that no single event would lead to acute radiation death if the aluminum spacecraft shielding exceeds 5 $g \cdot cm^{-2}$.

Despite the relatively low fluxes of GCR particles, long exposure times to a constant background radiation of GCR can result in a significant radiation dose accumulated during the entire flight, resulting in dangerous biological effects. Shielding from GCR is a challenging task due to the high energies of the particles (Figure 1a). The high kinetic energies result in a high penetration ability and a large amount of energy being deposited in tissues and organs. In addition, space radiation particles produce significant amounts of secondary particles while propagating through the spacecraft shielding due to nuclear interactions with the shielding materials. These additional secondary particles propagate into the spacecraft interior and increase the radiation dose. For shields with the same surface densities, the number of secondary particles and associated radiation damage is higher for shields made of materials with high atomic number (Z) elements. For example, it has been shown experimentally that for 10^3MeV $\cdot$ nucleon^{-1} iron ions, the radiation damage is reduced for low-Z materials such as polyethylene, and increased for high-Z materials such as lead (Durante & Kronenberg, 2005).

The results of the simulation (Slaba et al., 2017) performed with the High charge (Z) and Energy TRaNsport (HZETRN) code (Norbury et al., 2019; Wilson et al., 2014) for a 1 mm thick water slab placed between two plates of aluminum shielding, have shown that the dependence of the dose equivalent on the aluminum shielding thickness has a local minimum at 20 $g \cdot cm^{-2}$. However, 1 mm water slab is too thin to represent the human body. For a 30 cm water slab, which is a more realistic surrogate of human body, these calculations show a monotonic decay of the radiation dose with an increase in shielding thickness without a local minimum.

While most studies performed with HZETRN are focused on how the received dose changes with thickness for a specific phase of the solar cycle, the GCR dose evolution between 1997 and 2014 in the near-Earth interplanetary space was calculated (Mrigakshi et al., 2013) with the GEANT4 Monte Carlo code. The simulation shows a local minimum in the thickness dependence of the dose equivalent between 0.3 and 40 $g \cdot cm^{-2}$ during the 2001 solar max and an absence of such a minimum during the 2010 solar min. The simulations were performed for a spherical water phantom with a 25 cm radius, placed in the center of a spherical aluminum shell.

The biological effect of space radiation cannot be characterized just by the value of dose absorbed in each type of tissue, expressed in units of gray (Gy). The damage in biological tissue also depends on the ionization density along the particle track, which in turn changes with particle energy and type. The radiation damage to different organs is characterized by the dose equivalent, and for the entire organism, by the effective dose. The dose equivalent and the effective dose are both expressed in the units of sievert (Sv). Policies issued by space agencies use effective dose value to regulate astronauts' activity. One of the most accepted thresholds for acceptable dose is 1 Sv. The Russian Space Agency uses it as a career limit for whole-body exposure (Agency, 2004), which guarantees a total radiation risk at a level of 10%. In NASA regulations (Richard & Williams, 2015), exposure limits are defined separately for cancer-induced mortality and for non-cancer effects. The cancer-induced limits depend on the mission duration and the astronaut's age and gender, and keep the probability of the radiation-induced death within 3% with a 95% confidence level. The overall exposure for an astronaut should fulfill all requirements. We will use the value of 1 Sv to analyze an interplanetary flight, although the limit is established for the low-Earth orbit missions. The reason is the absence of regulations for upcoming interplanetary flights. Additionally, recent results (Zeitlin et al., 2019) demonstrate the similarity of the radiation environment on low-Earth orbit and for interplanetary flight. If the dose limits were to be reconsidered in the future, the results presented in this paper can be easily used to estimate new limits of the mission duration, while conclusions about the optimal flight conditions would not change.

Most previous studies provided estimations of the radiation doses during solar cycle activity maxima and/or minima, and during the strongest SEP events. Several studies considered radiation doses during 500- and 1000-days flights, according to NASA plans (Drake et al., 2009). However, there is still no clear answer about optimal flight conditions that would enable the longest mission duration. In this study, we present the net radiation doses from SEP and GCR radiation as an accumulated dose during a spaceflight, dependent on flight duration and launch date for the time period between 1998 and 2006. For this purpose, using the GEANT4 Monte Carlo code, we calculate the radiation dose distribution inside a spherical water phantom and the dependence of the dose and dose composition on the flight conditions (thickness of spherical aluminum shielding and phase of solar cycle). We show that the minimum radiation dose will be obtained for a flight launched during solar max behind an aluminum shield with a thickness of 30 $g \cdot cm^{-2}$. Furthermore, we demonstrate that the position of a local minimum in the dependence of the effective dose on the thickness of shielding depends on the solar activity, and a further increase in shielding beyond this optimal value results in an increase in effective dose. Our simulations show that for solar cycle 23 and aluminum shielding, the mission duration–assuming a 1 Sv mission limit–should not exceed approximately 4 years.

2. Modeling Methodology

In this study, we model the propagation of high-energy particles through a spacecraft shell containing an astronaut phantom to calculate the doses from GCR and SEP during an interplanetary flight. We use a spherical water phantom with an outer radius of 17.5 cm and a spherical cavity inside with a radius of 5 cm as an

astronaut phantom, which is similar to the phantom used in the MATRESHKA-R experiment (Shurshakov et al., 2014). As a spacecraft model, we use a spherical aluminum shell with a 1 m inner radius. The outer radius is varied according to the desired spacecraft shell thickness. The phantom is located in the center of aluminum shell, as illustrated in Figure 1b. This illustration shows, how primary GCR protons (depicted as blue lines) with energy of ~3 GeV (which is median energy for GCR proton spectrum) propagate from the left edge of the figure to the right, hit the shielding and phantom (interaction points are shown with red dots), and produce a lot of secondary particles (see caption for the details) in the aluminum shell. We discuss advantages of the spherical geometry in details in Appendix A. We use the GEANT4 Monte Carlo code (Agostinelli et al., 2003) v4.10.05.p02 to simulate particle propagation through the spacecraft shell and energy deposition in the phantom. Particle-matter interactions are described with the FTFP_BERT_HP physical processes list, which is recommended for high-energy particle physics applications (GEANT4 Reference Physics Lists, 2021). Physical models include the Fritiof model for particles with energies higher than 10 GeV, the Bertini Cascade model for energies lower than 10 GeV, and the High Precision Neutron model for energies lower than 20 MeV. Calculations with a different list of physical processes (FTFP_BERT_HP, QGSP_BERT_HP, and QGSP_INCLXXX_HP) could provide a slightly different result within 5% according to test calculations.

To account for the solar-cycle dependence of the GCR flux, we use a model (Matthiä, Berger, Mrigakshi, & Reitz, 2013), which takes into account the sunspot numbers between 1997 and 2012, and allows for a more straightforward comparison with the results of previous studies. The model describes ion spectra from hydrogen to nickel (Figure 1a) and is driven by the Wolf sunspot number. To describe SEP, we use spectra of the strongest SEP events from August 1997 to 2006, obtained with instruments on the Geostationary Operational Environmental Satellite (GOES) and the Advanced Composition Explorer (ACE) satellite (Evaluated Solar Energetic Particle Data, 2018). The SEP particle flux depends on the particle type and is highest for protons. SEP spectra (cyan, green, and black curves on Figure 1a) are considered for energies from 10 MeV $\cdot$ nucleon^{-1} to 10^3 MeV $\cdot$ nucleon^{-1}. Intensities reach a maximum value at 10 MeV $\cdot$ nucleon^{-1} and decrease with increasing energy. It is worth mention that SEP protons with higher energy up to 2 GeV increase the radiation dose by ~ 2% in average (Mertens & Slaba, 2019).

We use the "response function" approach to calculate the radiation dose. The "response function" is the dependence of the radiation dose deposited with space radiation particle on the particle type and energy. First, we calculate the "response function" modeling the spacecraft shell irradiation with 28 fully ionized particles from hydrogen to nickel. We consider primary particles with an initial energy from 7 MeV $\cdot$ nucleon^{-1} to 128 GeV $\cdot$ nucleon^{-1} as most of the particles have energies in this range (Figure 1a). The energy range is divided into 21 bins on a logarithmic scale. The energy distribution inside each bin is flat. A large number of simulation runs, more than $4 \cdot 10^5$, are performed for every geometry, particle, and energy combination. In a single simulation run, the propagation of one primary particle is modeled. We vary the number of simulation runs to keep a balance of calculation time and precision of the result (see Appendix B).

In the second step, we calculate the radiation dose for a particular radiation environment as a convolution of space radiation spectra with the "response function." We multiply the particle flux value in an energy bin by the corresponding radiation dose value of the "response function." The sum of the dose over all bins provides the net dose. The main advantage of this method is that the Monte Carlo simulations need to be done only once. Afterward, the radiation dose for a particular spectrum can be easily calculated.

We consider the irradiation of the spacecraft with SEP and GCR particle flux as isotropic and homogeneous. A spherical omnidirectional particle source with a radius much larger than the spacecraft shell creates an isotropic flux on the surface of a spherical shell. However, most of the particles, in this case, do not collide with the spacecraft shell. To avoid unnecessary calculations for particles not encountering the spacecraft, in this study we use a planar circular source with a radius equal to the outer radius of the shield shell. In doing so, we create the same angular distribution of incident particles on the shell surface as a large spherical isotropic source. This approach requires applying a scaling coefficient when the particle flux value is calculated. The advantage of this setup is that all particles collide with the shield shell. Another advantage is that all primary particles propagate in one direction. This simulation set up makes it easier to distinguish between secondary particles propagating in forward (having the velocity component along the initial direction of primary particles) and backward directions (having the velocity component opposite to the initial direction of

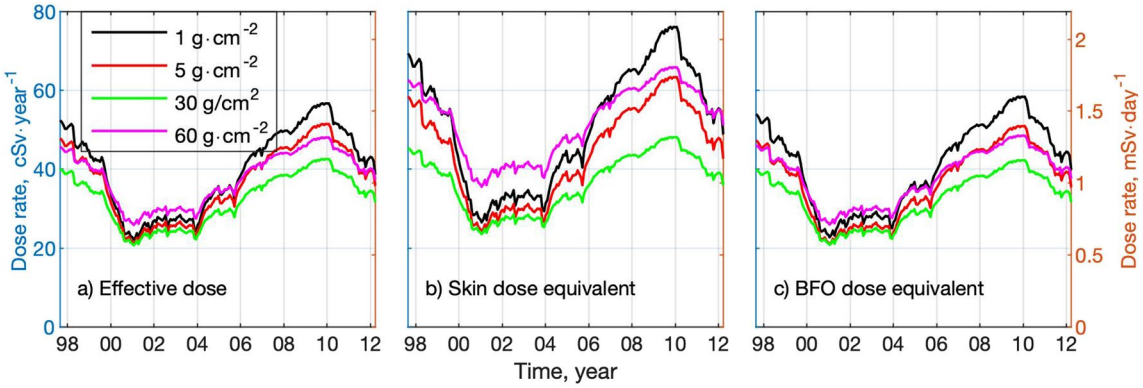

Figure 2. Time-dependence of Galactic Cosmic Rays (GCR) effective dose and dose equivalent for different shielding thicknesses (indicated by the different colors). Panel (a) shows the dependence of the effective dose, (b) the dependence of the skin dose equivalent (0.5 mm layer at the surface of the phantom), (c) the dependence of the blood forming organ dose equivalent (1 mm layer at 2.5 cm under the phantom surface).

primary particles). In Appendix D, we present the contribution of different radiation components (primary, secondary forward propagating, secondary backward propagating, and multipass) to the net dose and their dependencies on the shielding thickness.

The outputs of our modeling framework are distributions of the absorbed dose and dose equivalent in the phantom. Energy deposition inside the phantom is detected in 126 spherical layers with a thickness of 1 mm, except for the innermost and outermost layers, which have thicknesses of 0.5 mm.

We calculate the radiation dose equivalent in each layer following the guidelines from the International Commission on Radiological Protection (ICRP, 1991) to characterize the biological effect of the radiation exposure. For each event of energy deposition, the absorbed energy is multiplied by a quality factor dependent on linear energy transfer (LET). The LET represents the ionization density along the particle track and is calculated by dividing the deposited energy by the track length for each part of the particle track. The absorbed dose and dose equivalent are calculated by summing corresponding values over the volume of interest and dividing by the mass of the volume.

The career exposure limits for astronauts are defined for the effective dose, which is calculated as the sum of the dose equivalent in 15 critical organs (ICRP, 2007) multiplied by corresponding weighting factors. Out of 126 layers of our phantom we select 15 that correspond to critical organs following the procedure based on matching mean values of self-shelding, as described in a study (Matthiä, Berger, & Reitz, 2013).

3. Results of Simulations

Figure 2 shows the time dependencies of GCR doses from 1998 to 2012, behind aluminum shielding of different thickness. The skin dose equivalent is detected in the 0.5 mm surface layer of the phantom. The Blood Forming Organs (BFO) dose equivalent is detected in the 1 mm spherical layer located 2.5 cm under the phantom surface. Both the effective dose and dose equivalent decrease when the shielding is increased from 1 $g \cdot cm^{-2}$ to 20–30 $g \cdot cm^{-2}$. A further increase in the shielding results in an increase in the GCR dose. A detailed comparison of the dependencies of the effective dose on shielding thickness is presented in the appendix material. It should be noted that GCR variations due to solar activity are different at different energies (Figure 1a). The effect of these differences on the effective dose is shown in Figure C1 and discussed in Appendix C.

Figure 3a shows the thickness-dependence of the GCR effective dose during solar max (red circles) and solar min (blue squares). Both dependencies exhibit a minimum. The minimum is located at 30 $g \cdot cm^{-2}$ during solar min and 20 $g \cdot cm^{-2}$ during solar max. During solar max use of shielding thicker than 40 $g \cdot cm^{-2}$ results in a higher dose than for negligible shielding.

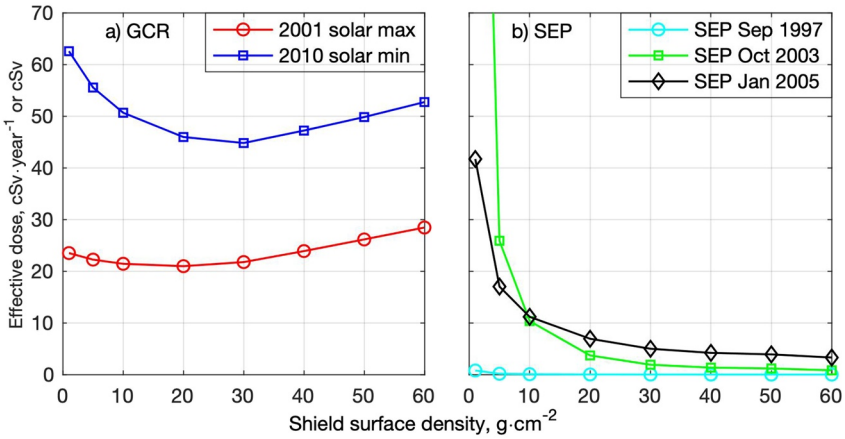

Figure 3. (a) Dependence of the galactic cosmic rays (GCR) effective dose on the shielding thickness in units of cSv · year^{-1}. (b) Dependence of the solar energetic particles (SEP) effective dose in units of cSv on the shielding thickness for three "typical" solar particle events.

Figure 3b presents the dependence of the effective dose on the shielding thickness for three selected SEP events. Note that the *y*-axis shows the total dose per event, while Figure 3a shows the dose rate per year from GCR radiation exposure. Dose calculations are presented for three SEP events: (a) September 1997, (b) October 2003, and (c) January 2005. For all three SEP events, the effective dose decreases monotonically with increasing thickness of shielding. Even for thin shielding, the effective dose from GCR over 1 year exceeds the dose from "weak" SEP (cyan curve), which occur most frequently. For all considered SEP events, the effective dose due to SEP is lower than the "annual" GCR dose behind shielding of 5 g · cm^{-2} or greater. Note that the effect of SEP depends on the particle spectra, and SEP with soft spectra (green curve) result in a higher dose behind thin shielding, while SEP with hard spectra (black curve) may produce a significant dose behind thick shielding. Figure 4 shows the accumulated effective dose from both GCR and SEP as a function of the launch date and mission duration. These dependencies include 56 SEP events during the time period from 1997 to 2006. For each solar event, the fluence spectra of hydrogen, helium, carbon, nitrogen, oxygen, neon, magnesium, silicon, sulfur, and iron ions are considered.

The SEP deposit a very large dose of radiation in the phantom when it is lightly shielded (Figure 4a). The radiation dose behind a 1 g · cm^{-2} shielding will exceed 1 Sv after one solar event. However, such a low shielding scenario is unrealistic and can only be used to model the extravehicular activity, which makes up a small proportion of an astronaut's time in space. For 5 g · cm^{-2} shielding (Figure 4b), the SEP contribution becomes small, but 1 Sv is reached within approximately 2 years for a launch between 2001 and 2003. Behind thicker shielding, the contribution of GCR becomes larger than that of SEP.

While the minimum in the GCR-induced effective dose during solar max is reached behind 20 g · cm^{-2}, the combined effect of GCR and SEP is minimized behind 30 g · cm^{-2} shielding. The longest time to reach 1 Sv for the optimal shielding of 30 g · cm^{-2} is 3.8 years and is reached for a mission launched in 2001 during solar max (Figure 4c). Our calculations show that shielding of 60 g · cm^{-2} (Figure 4d) has approximately the same efficiency as that of 30 g · cm^{-2}, but the neutron component in the net dose is larger by a factor of approximately 2, compared to the 30 g · cm^{-2} shielding (see Appendix E).

4. Discussion

The dependencies of dose on thickness shown on Figure 2a can be compared to modeling results (Mrigakshi et al., 2013) that use a similar simulation methodology. The effective dose in our calculation is ~10% higher compared to the average dose equivalent since the effective dose is calculated using the outer layers, which have higher dose equivalent values. A good agreement in the average dose equivalent is achieved for small shielding thicknesses up to 10 g · cm^{-2}. Both simulations predict that the dose equivalent during

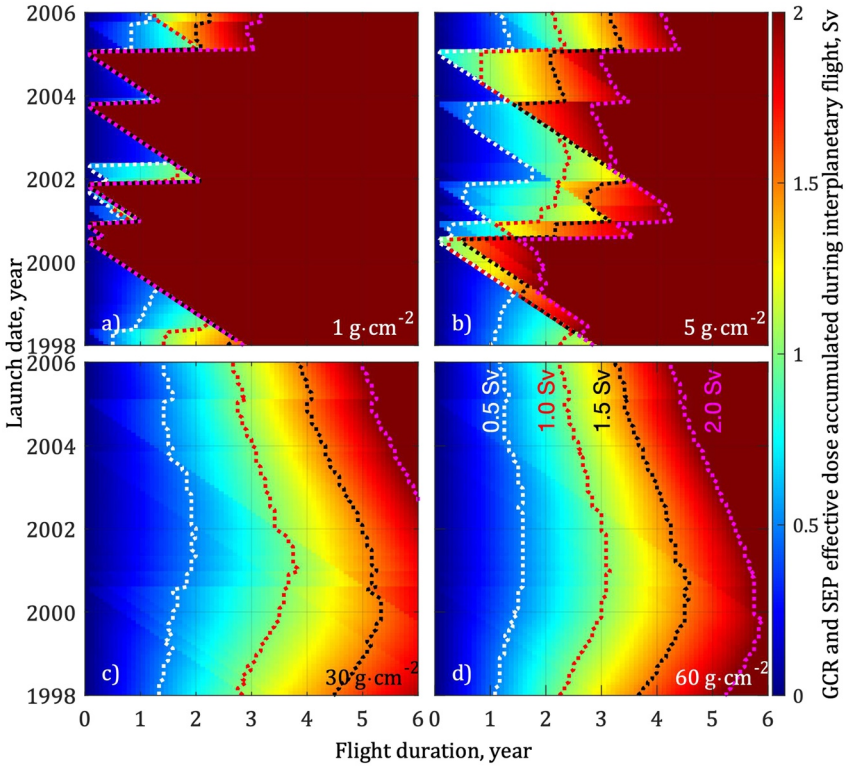

Figure 4. Dependence of the net effective dose accumulated during an interplanetary flight on the mission duration (x axis) and launch date (y axis). Panel (a) shows the dose dependence behind shielding of 1 g · cm^{-2}; panel (b) 5 g · cm^{-2}, (c) 30 g · cm^{-2}, and (d) 60 g · cm^{-2}. Dotted curves show levels of 0.5 Sv (white), 1 Sv (red), 1.5 Sv (black), and 2 Sv (magenta), respectively.

solar min decreases when the shielding is increased up to 30 g · cm^{-2}. There were small differences in the dose equivalent behind shielding thicker than 30 g · cm^{-2}, that can be potentially could be attributed to the differences in the simulation methodology.

The position of the local minimum of radiation dose in Figure 3a differs from the 40 g · cm^{-2} to 20 g · cm^{-2} reported previously (Slaba et al., 2013, 2017). These differences may be related to the differences between the models of GCR used for the calculations. It is not clear if there is a difference in the dose minimum position in the results (Mrigakshi et al., 2013), as calculations were not performed for thicknesses between 10 g · cm^{-2} and 40 g · cm^{-2}.

In this study, we considered only aluminum shielding. Composite materials including hydrogen-rich composites have often been discussed for use in deep space habitats. Materials such as a carbon composite with significant hydrogen content may potentially improve shielding and allow for longer flight times, as materials containing light elements result in lower fluxes of secondary particles. In particular, the presence of light elements may decrease the flux of neutrons that contribute 20%–50% of the equivalent dose (Figure E1). While the use of such materials can increase the allowed flight time, the increase will depend on the material used, but most likely will not exceed a 20% improvement in the effective shielding, which will add no more than one additional year of flight time.

In this study, we refer to the 1 Sv value of whole-body exposure as the career dose limit for astronauts. While this is the criterion that is, currently most widely adopted by space agencies, future radiobiological studies may set up lower or higher standards, and the exact conclusions of this study can be revised accordingly. It should be noted that the exact length of the suggested mission duration may change as we learn more about biological effects and develop new materials. However, this study provides the most realistic estimate of the mission duration, for currently used materials and estimates of the limiting radiation doses.

It should be noted that solar cycles can significantly vary (Schwadron et al., 2014), and it is currently not possible to predict the strength of future solar cycles. The dose for a solar cycle that is weaker than the ones considered here can increase the GCR-induced dose, which in turn will increase the net dose. This study provides the first realistic ballpark estimate of the duration of the mission to Mars, a feat that is certainly challenging but is still possible.

5. Conclusions

In this study, we combined models of the space environment with simulation results of radiation particle propagation through a spacecraft model with various aluminum shielding thicknesses, and estimated the effective dose and dose equivalent for an astronaut during a long-term interplanetary flight. We considered a spherical water phantom in a spherical spacecraft shell, and analyzed how the radiation dose absorbed in the phantom depends on the aluminum spacecraft shielding thickness (surface density values of 0, 5, 10, 20, 30, 40, 50, and 60 $g \cdot cm^{-2}$).

The results shown in this study can be translated into general recommendations for spacecraft designer and for mission planing. First, a long-duration mission should be scheduled only for the period of solar max to reduce the influence of GCR radiation. Second, spacecraft shielding should be thick enough (~20–30 $g \cdot cm^{-2}$) for efficient attenuation of SEP radiation but should not be thicker than ~30 $g \cdot cm^{-2}$ to prevent the production of secondary particles, especially neutrons (see Appendix F).

The shortest Earth–to–Mars flight times will be in 2030 and 2050, corresponding to periods of solar max. Current work shows that for the previous solar cycle, the smallest effective dose would have been accumulated for a flight starting in 2000, during solar max. For an optimal average shielding of 30 $g \cdot cm^{-2}$, the effective dose would be 0.5 Sv after a 1.9-years flight and astronaut's career dose limit of 1 Sv would be accumulated after a 3.8-years flight.

Appendix A: Advantages of Spherical Geometry

The shielding geometry used for dose calculation plays a significant role, and most studies looking for optimal shielding simplify the geometry using models. The most common homogeneous shielding models use either slab shielding geometry or spherical geometry. With regard to calculating GCR radiation doses, spherical shielding geometry appears to be preferable for two reasons: the nominal shield thickness is passed only by particles that propagate toward the center, and as the majority of particles propagate in different directions the actual shield thickness would be higher. Therefore, the attenuation of primary particles and the production of secondary particles would be different resulting in different contribution to the dose equivalent (Dobynde & Shprits, 2020). Barthel and Sarigul-Klijn (2019) demonstrated the differences in the particle flux behind the slab and spherical shielding using the HZETRN calculations and outline the importance of spherical geometry for valid assessment of neutron dose. Additional advantage of spherical geometry is accounting the free space between the phantom and inner surface of the shielding, which is generally omitted in the slab geometry shielding models. If there is no free space between shielding and the phantom, all secondary particles induced in the shield hit into the phantom. The size of free space has significant influence on the radiation dose composition (Dobynde & Shprits, 2020), even if the shielding thickness and the net dose values are the same.

The spherical water phantom is a convenient (GOST-18622-79, 2003; Mrigakshi et al., 2013; Wilson et al., 2015) simplification of the human phantom. The main advantage is that one set of calculations provides a dose distribution inside the phantom, and the effect of self-shielding is taken into account. In accordance with the average shielding value, radiation doses at different depths can be attributed to doses in the anthropomorphic phantom (Matthiä, Berger, & Reitz, 2013). Radiation doses calculated in a thin water slab behind different shielding, known as depth-dose curves, are used as input data for radiation dose shield-function methodology calculations, and can be used only as an estimation of skin-dose as the effect of body self-shielding is omitted. This can be observed in radiation dose HZETRN calculations (Slaba et al., 2017) that are dependent on shielding thickness, when the local minimum is seen for a 1 mm water slab detector and is absent in the case of a 30 cm water slab detector.

Appendix B: Stability of Monte Carlo Solution

In calculations with a spherical geometric setup, the standard deviation cannot be used to evaluate calculation errors as it is in the order of, and at times exceeds the mean value. This can be attributed to the differences in particle track length in the phantom, as particles that propagate closer to the center of the phantom would deposit much more energy than particles propagating closer to the phantom boundary. We decided to use a normalized mean dose deviation as the criteria for result convergence. Namely, we use the value of normalized deviation Δ, which is calculated on iteration N+1 as:

$$\Delta_N = \frac{\Delta_{N+1} - \Delta_N}{\Delta_{N+1} + \Delta_N} \tag{B1}$$

where Δ_{N+1} is the average dose after the (N+1)th iteration, and Δ_N is the average dose after the Nth iteration. We start calculating the normalized deviation on the 1,001 iteration. As soon as Δ holds at less than 0.001 during 1,000 iterations, we assume that we have obtained a stable solution.

Thus, the minimum iteration number is 2,000, while the maximum is set to keep particle density on the source surface equal to 40 cm^{-2}. For the smallest shielding thickness of 1g $\cdot$ cm^{-2}, the maximal number is 403,000 and for 60 g $\cdot$ cm^{-2} shielding, the number is 598,000.

Appendix C: Dependence of Effective Dose on Particle Energy

The effective dose during solar max has a weak minimum at 20 g $\cdot$ cm^{-2} (Figure C1a), however during solar min, the minimum is at 30 g $\cdot$ cm^{-2} and is more pronounced. The radiation particle spectra determine the dependencies of dose on shielding thickness. The variation of the GCR spectra on the phase of the solar cycle is more substantial for low-energy particles than for high-energy particles. To examine the influence of the GCR spectra on the effective dose, we divided the GCR particles into the three groups shown in Figure C1: (a) Particles with energies lower than 0.3 GeV $\cdot$ $nucleon^{-1}$ (red curves), (b) particles with energies between 0.3 and 5 GeV $\cdot$ $nucleon^{-1}$ (blue curves), and (c) particles with energies higher than 5 GeV $\cdot$ $nucleon^{-1}$ (green curves). The variations in the GCR spectra (Figure C1a) are significant for "low"-energy particles, moderate for "mid"-energy particles, and insignificant for "high"-energy particles. These features are reflected in the corresponding dependencies of the effective dose on the shielding thickness. The effective dose due to the "high"-energy particles (green curves) is almost the same during solar min than solar max. It increases in relation to shielding thickness due to secondary particle production. The effective dose due to the "low"-energy particles (red curves) is significantly higher during solar min than during solar max. It decreases with the increase in shielding thickness due to the absorption of primary particles and a small number of secondary particles. The effective dose due to the "mid"-energy particles (blue curves) is twice as high during solar min compared with the solar max. It has a weak minimum at 30 g $\cdot$ cm^{-2}, which is the result of attenuation of primary particles and production of secondary particles.

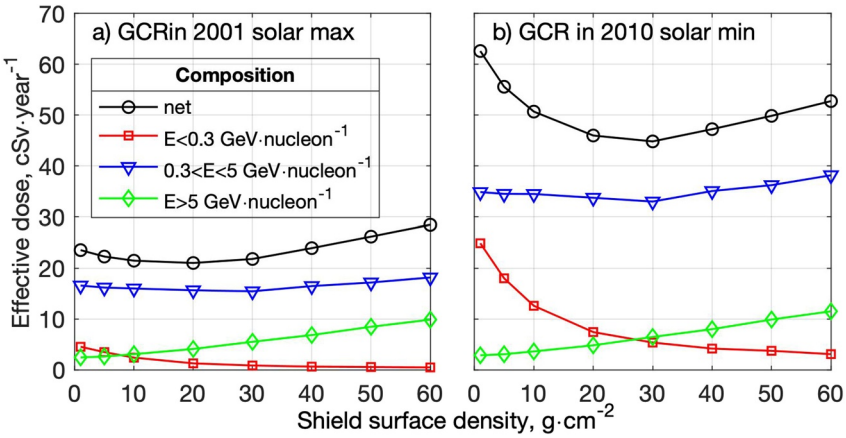

Figure C1. Galactic cosmic rays (GCR) effective dose as a function of the thickness of shielding during solar max (panel a), and during solar min (panel b). The net dose is shown in black; colored curves show effective dose due to particles from three energy ranges, according to the legend.

In summary, the double effective dose average difference due to the GCR in the solar min and solar max is due to the "mid"-energy particles, while the position of the minimum is the result of variation in "low"-energy particle spectra.

Appendix D: Dose Composition

While the SEP radiation dose is mostly due to primary particles, secondary particles significantly contribute to the GCR radiation dose. All particles are divided into four groups: (a) primary particles; (b) secondary particles propagating forward and having a velocity component along the initial direction of primary particles; (c) secondary particles propagating backward and having a velocity component opposite to the initial direction of primary particles; and (d) secondary multipass particles, that pass through the phantom two or more times. We refer to primary particles as the particles launched from the source and secondary particles as the particles that pass into the phantom which are not primary. Figure D1 shows the contribution of primary, forward propagating, backward propagating, and multipass particles to the net dose equivalent.

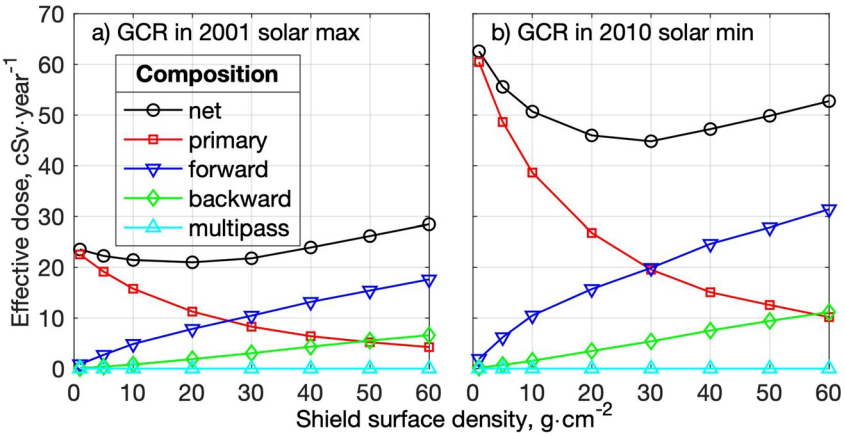

Figure D1. Dependence of the effective dose on shielding thickness during the 2001 solar max (panel a) and the 2010 solar min (panel b). The net dose is shown in black; colored curves show effective dose due to four species of particles according to the legend.

Figure D1 demonstrates that the net GCR effective dose is lower during solar max (black curves). There are also several features that are common to both panels. The first is that the primary particle contribution (red curves) decreases monotonically with an increase of shielding thickness. The second is that the contribution of secondary (blue and green curves) particles monotonically increases with an increase in shielding thickness. It is also worth noting that the radiation dose from multipass particles (cyan curves) increases with thicker shielding, but is much lower than the other components.

Appendix E: Dose Distribution Inside the Phantom

Figure E1 shows the distribution of the dose equivalent inside the phantom. Looking at continuous inward increments of 1 mm depth inside the phantom, the volume of spherical layers decreases, and the number of particles per considered volume is smaller and reaches counting statistics. This may explain oscillations seen at a depth of ~5 cm and more.

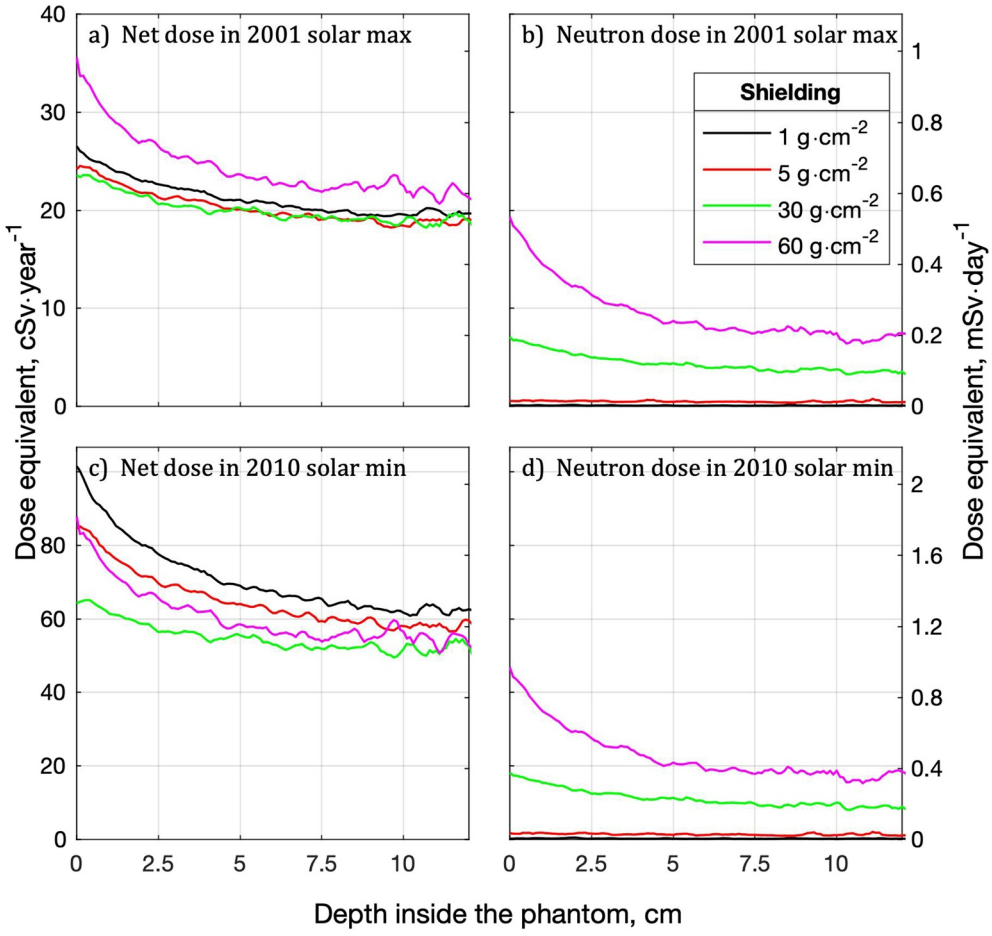

Figure E1. Depth distribution of galactic cosmic rays (GCR) dose equivalent inside a water phantom behind shielding of different thickness. Panels (a and b) show the dependence during solar max and panels (c and d) during solar min. Panels (a and c) illustrate the distribution of the net dose, whereas panels (b and d) show the distribution of the secondary neutron dose.

The net dose equivalent (Figures E1a and E1c) decreases with depth inside the phantom irrespective of chosen thicknesses of shielding. It can be seen that the net dose distribution (Figures E1a and E1c) behind any shielding during solar max (Figure E1a) is lower than the radiation dose distribution behind the thickest shielding during solar min (Figure E1c). The dose of secondary neutrons increases by a factor of two during solar min (Figures E1b and E1d), when the GCR flux is significantly increased in comparison to solar max.

The net dose decreases with an increase of thickness of shielding up to 30 $g \cdot cm^{-2}$, whereas the dose of secondary neutrons (Figures E1b and E1d) increases for all selected thicknesses of shielding. The dose of secondary neutrons is two times higher behind 60 $g \cdot cm^{-2}$ shielding compared to 30 $g \cdot cm^{-2}$. During the solar min in 2010, behind 60 $g \cdot cm^{-2}$ shielding, secondary neutrons contributed more than ~53% of the net dose for skin, up to ~43% for BFO (2.5 cm depth), and up to ~37% for deeper (greater than 10 cm depth) phantom regions. Most of the dosimeters are sensitive to charged particles; thus, the measured dose can be significantly lower than in reality and may underestimate the risk for an astronaut's health. Therefore, it is of vital importance to develop and implement dosimeters sensitive to neutrons.

Appendix F: Effective Dose Composition

Figure F1 shows the effective dose dependence on the shielding thickness and contribution of secondary particles of different species to the net dose. It can be seen that the primary particle contribution decreases with increasing shielding thickness, while the secondary particle contribution increases. Our calculations indicate that most of these secondary particles is induced with GCR protons and alpha particles, which is in a good agreement with previous results (Slaba & Blattnig, 2014). Among the secondary particles, the highest contribution to the effective dose is due to secondary neutrons and protons. The secondary nucleons shown in cyan are mostly HZE fragments in our calculations are considered as secondary particles.

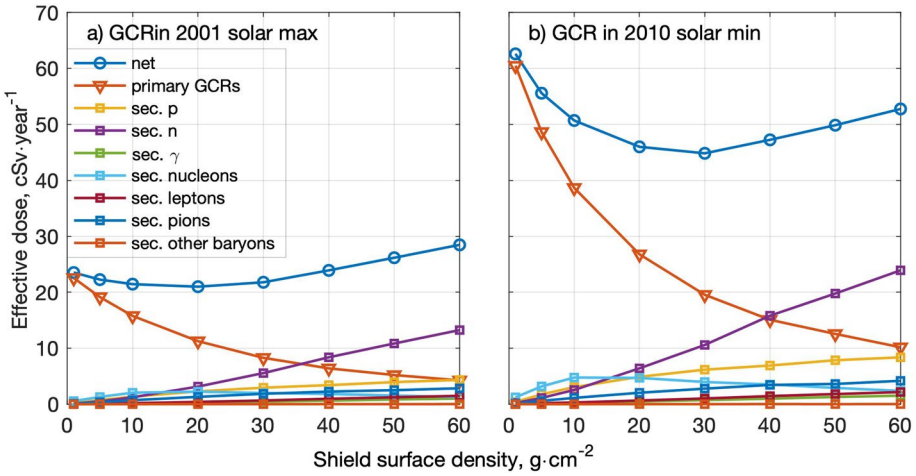

Figure F1. Dependence of the galactic cosmic rays (GCR) effective dose on the thickness of aluminum shielding during the period of the 2001 solar max (a) and 2010 solar min (b). Dependencies for different particle species are shown in different colors or markers according to the legend.

Data Availability Statement

The resulting data sets of this study are available at https://doi.org/10.5281/zenodo.5148742.

Acknowledgments
This work used computational and storage services associated with the Hoffman2 Shared Cluster provided by the UCLA Institute for Digital Research and Education's Research Technology Group. The authors used solar energetic particle spectra from the Skobeltsyn Institute of Nuclear Physics website (http://dec1.sinp.msu.ru/models/sep/db/). The authors appreciate Dr. Dominika Soergel's help with reviewing the manuscript text.
Open access funding enabled and organized by Projekt DEAL.

References

Agency, R. F. S. (2004). *Imitation of astronaut's exposure during near-Earth space flights, methodical recommendations*. MR 2. 6. 1.44-03-2004.
Agostinelli, S., Allison, J., Amako, K., Apostolakis, J., Araujo, H., Arce, P., & Zschiesche, D. (2003). GEANT4 - A simulation toolkit. *Nuclear Instruments and Methods in Physics Research Section A: Accelerators, Spectrometers, Detectors and Associated Equipment*, *506*(3), 250–303. https://doi.org/10.1016/S0168-9002(03)01368-8
Barthel, J., & Sarigul-Klijn, N. (2019). Importance of spherical shell models for radiation shielding designs on space missions. *Journal of Spacecraft and Rockets*, *56*(5), 1658–1661. https://doi.org/10.2514/1.a34410
Cucinotta, F. A., Kim, M. H. Y., Chappell, L. J., & Huff, J. L. (2013). How safe is safe enough? Radiation risk for a human mission to Mars. *PloS One*, *8*(10), e74988. https://doi.org/10.1371/journal.pone.0074988
Dobynde, M. I., & Shprits, Y. Y. (2020). Radiation environment created with GCRs inside a spacecraft. *Life Sciences in Space Research*, *24*(August), 116–121. https://doi.org/10.1016/j.lssr.2019.09.0011
Drake, B. G., Hoffman, S. J., & Watts, K. D. (2009). *Human exploration of Mars design reference architecture 5 .0 addendum #2*. Nasa(March). https://doi.org/10.1109/AERO.2010.5446736
Durante, M., & Kronenberg, A. (2005). Ground-based research with heavy ions for space radiation protection. *Advances in Space Research*, *35*(2), 180–184. https://doi.org/10.1016/j.asr.2004.12.034
Evaluated solar energetic particle data. (2018). Retrieved from http://dec1.sinp.msu.ru/≈chapai/projects/database/
Forbush, S. (1958). Cosmic-ray intensity variations during two solar cycles. *Journal of Geophysical Research*, *63*, 651–669. https://doi.org/10.1029/jz063i004p00651
Geant4 reference physics lists. (2021). Retrieved from https://geant4.web.cern.ch/node/302
Golge, S., O'Neill, P. M., & Slaba, T. C. (2015). NASA galactic cosmic radiation environment model: Badhwar - O'Neill (2014). In *International Cosmic Ray Conference (ICRC)*. Proceedings of Science, 30-July-20.
GOST-18622-79. (2003). *Interaction of ionizing radiation with matter. Chemical composition of the tissue-equivalent matter* [in Russian]. GOST-18622-79.
Hassler, D. M., Zeitlin, C., Wimmer-Schweingruber, R. F., Ehresmann, B., Rafkin, S., Eigenbrode, J. L., & Grotzinger, J. P. (2014). Mars' surface radiation environment measured with the Mars science laboratory's curiosity rover. *Science*, *343*(6169), 1–11. https://doi.org/10.1126/science.1244797
Hu, S., Kim, M.-H. H. Y., McClellan, G. E., & Cucinotta, F. A. (2009). Modeling the acute health effects of astronauts from exposure to large solar particle events. *Health Physics*, *96*(May), 465–476. https://doi.org/10.1097/01.HP.0000339020.92837.61
ICRP. (1991). 1990 recommendations of the international commission on radiological protection. *Annals of the ICRP*, *21*(1–3).
ICRP. (2007). The 2007 recommendations of the international commission on radiological protection. ICRP publication 103. *Annals of the ICRP*, *37*(2–4).
Matthiä, D., Berger, T., Mrigakshi, A. I., & Reitz, G. (2013a). A ready-to-use galactic cosmic ray model. *Advances in Space Research*, *51*(3), 329–338. https://doi.org/10.1016/j.asr.2012.09.022
Matthiä, D., Berger, T., & Reitz, G. (2013b). Organ shielding and doses in Low-Earth orbit calculated for spherical and anthropomorphic phantoms. *Advances in Space Research*, *52*(3), 528–535. https://doi.org/10.1016/j.asr.2013.03.025
Mertens, C. J., & Slaba, T. C. (2019). Characterization of solar energetic particle radiation dose to astronaut crew on deep-space exploration missions. *Space Weather*, *17*(12), 1650–1658. https://doi.org/10.1029/2019SW002363
Mrigakshi, A. I., Matthiä, D., Berger, T., Reitz, G., & Wimmer-Schweingruber, R. F. (2013). Estimation of galactic Cosmic ray exposure inside and outside the Earth's magnetosphere during the recent solar minimum between solar cycles 23 and 24. *Advances in Space Research*, *52*(5), 979–987. https://doi.org/10.1016/j.asr.2013.05.007
Norbury, J. W., Slaba, T. C., Aghara, S., Badavi, F. F., Blattnig, S. R., Clowdsley, M. S., & Zeitlin, C. (2019). Advances in space radiation physics and transport at NASA. *Life Sciences and Space Research*, *22*(April), 98–124. https://doi.org/10.1016/j.lssr.2019.07.003
Nymmik, R. A., Panasyuk, M. I., Pervaja, T. I., & Suslov, A. A. (1992). A model of galactic cosmic ray fluxes. *International Journal of Radiation Applications and Instrumentation Part A*, *20*(3), 427–429. https://doi.org/10.1016/1359-0189(92)90028-T
Nymmik, R. A., Panasyuk, M. I., & Suslov, a. a. (1996). Galactic cosmic ray flux simulation and prediction. *Advances in Space Research: The official journal of the Committee on Space Research (COSPAR)*, *17*(2), 19–30. https://doi.org/10.1016/0273-1177(95)00508-C
Richard, S., & Williams, M. (2015). *NASA space flight human-system standard volume 1 Revision A: Crew health* (Vol. 1, p. 83).
Schwadron, N. A., Blake, J. B., Case, A. W., Joyce, C. J., Kasper, J., Mazur, J., & Zeitlin, C. (2014). Does the worsening galactic cosmic radiation environment observed by CRaTER preclude future manned deep space exploration? *Space Weather*, *12*(11), 622–632. https://doi.org/10.1002/2014SW001084
Shurshakov, V. A., Tolochek, R. V., Kartsev, I. S., Petrov, V. M., Nikolaev, I. V., Moskalyova, S. I., & Lyagushin, V. I. (2014). Study of dose distribution in a human body in international space station compartments with the tissue-equivalent spherical phantom. *Journal of Radiation Research*, *55*(suppl 1), i61. https://doi.org/10.1093/jrr/rrt220
Slaba, T. C., Bahadori, A. A., Reddell, B. D., Singleterry, R. C., Clowdsley, M. S., & Blattnig, S. R. (2017). Optimal shielding thickness for galactic cosmic ray environments. *Life Sciences in Space Research*, *12*, 1–15. https://doi.org/10.1016/j.lssr.2016.12.003
Slaba, T. C., & Blattnig, S. R. (2014). GCR environmental models I: Sensitivity analysis for GCR environments. *Space Weather*, *12*(4), 217–224. https://doi.org/10.1002/2013sw001025
Slaba, T. C., Mertens, C. J., & Blattnig, S. R. (2013). *Radiation shielding optimization on Mars*. Langley Research Center.
Wilson, J. W., Slaba, T. C., Badavi, F. F., Reddell, B. D., & Bahadori, A. A. (2014). Advances in NASA radiation transport research: 3DHZETRN. *Life Sciences in Space Research*, *2*(October), 6–22. https://doi.org/10.1016/j.lssr.2014.05.003
Wilson, J. W., Slaba, T. C., Badavi, F. F., Reddell, B. D., & Bahadori, A. A. (2015). 3DHZETRN: Shielded ICRU spherical phantom. *Life Sciences in Space Research*, *4*, 46–61. https://doi.org/10.1016/j.lssr.2015.01.002
Zeitlin, C., Hassler, D. M., Cucinotta, F. A., Ehresmann, B., Wimmer-Schweingruber, R. F., Brinza, D. E., & Reitz, G. (2013). Measurements of energetic particle radiation in transit to mars on the mars science laboratory. *Science*, *340*(6136), 1080–1084. https://doi.org/10.1126/science.1235989
Zeitlin, C., Narici, L., Rios, R. R., Rizzo, A., Stoffle, N., Hassler, D. M., & Spence, H. E. (2019). Comparisons of high-linear energy transfer spectra on the ISS and in deep space. *Space Weather*, *17*(3), 396–418. https://doi.org/10.1029/2018SW002103